Editorial Manager(tm) for Publications of the Astronomical Society of the Pacific
Manuscript Draft

Manuscript Number: 350084R1

Title: Target acquisition for MIRI coronagraphs

Article Type: Article

Corresponding Author: Céline Cavarroc,

Corresponding Author's Institution: CEA

First Author: Céline Cavarroc

Order of Authors: Céline Cavarroc; Anthony Boccaletti; Pierre Baudoz; Jérôme Amiaux; Mike Regan

Abstract: Coronagraphs are powerful instruments to reduce diffraction from a bright source in order to detect planets. Four coronagraphs will be installed in MIRI, the Mid-InfraRed Instrument of the James Webb Space Telescope. To further reduce the diffraction in addition to the coronagraph, a calibration of the residual speckle pattern can be obtained for instance with a reference star (or alternatively on the target star at a different roll angle). For this calibration to be accurate, the diffraction pattern of the two coronagraphic images must be as similar as possible. We study the accuracy of the star image positioning onto the coronagraph to reach acceptable performance: we proved that pointing reproducibility must be better than 5~mas~RMS per axis while the absolute pointing can be relaxed to 10~mas~RMS. The choice of algorithm is driven by the level of accuracy to be reached in the presence of a non-linear system like the coronagraph. We first study their bias, and then we estimate their sensitivity to different sources of noises in the context of MIRI. And finally, for practical matter, we derive the necessary exposure time to obtain the centroid on an actual star.

Target acquisition for MIRI coronagraphs

C. Cavarroc

DSM/IRFU/SAp, CEA/Saclay, F-91191 GIF-SUR-YVETTE

and A. Boccaletti and P. Baudoz

LESIA, Observatoire de Paris Meudon, 5 pl. J. Janssen, F-92195 MEUDON

and J. Amiaux

DSM/IRFU/SAp, CEA/Saclay, F-91191 GIF-SUR-YVETTE

and M. Regan

STScI, 3700 San Martin Dr., BALTIMORE, MD 21218, USA

ABSTRACT

Coronagraphs are powerful instruments to reduce diffraction from a bright source in order to detect planets. Four coronagraphs will be installed in MIRI, the Mid-InfraRed Instrument of the James Webb Space Telescope. To further reduce the diffraction in addition to the coronagraph, a calibration of the residual speckle pattern can be obtained for instance with a reference star (or alternatively on the target star at a different roll angle). For this calibration to be accurate, the diffraction pattern of the two coronagraphic images must be as similar as possible. We study the accuracy of the star image positioning onto the coronagraph to reach acceptable performance: we proved that pointing reproducibility must be better than 5 mas RMS per axis while the absolute pointing can be relaxed to 10 mas RMS. The choice of algorithm is driven by the level of accuracy to be reached in the presence of a non-linear system like the coronagraph. We first study their bias, and then we estimate their sensitivity to different sources of noises in the context of MIRI. And finally, for practical matter, we derive the necessary exposure time to obtain the centroid on an actual star.

1. Introduction

The James Webb Space Telescope (JWST) will address questions from the origin of the universe to the formation of stars and planetary systems. With a diameter of 6.57 m

and a spectral coverage from 0.6 μm to 28 μm, it will provide an unprecedented sensitivity. One of the objectives of MIRI, the Mid-InfraRed Instrument of the JWST (5 - 28 μm), is the direct detection of Extrasolar Giant Planets (EGPs) around young stars (Boccaletti et al. 2005). The solution proposed to reduce the diffracted light near the star is to use a coronagraph. In the context of MIRI, the Four Quadrant Phase Mask coronagraph (Rouan et al. 2000) (afterwards FQPM) was selected because of its very small inner working angle, an appreciable characteristic at such wavelengths. The FQPM is theoretically perfect but owing to the aberrations of the telescope, the segmentation and the obstruction of the primary, the raw contrast is not sufficient to detect EGPs. To improve the signal-to-noise ratio and thus the detectability of EGPs, the coronagraphic image residuals have to be calibrated. This can be obtained by different means: using angular differential imaging where the target star is observed with different roll angles of the telescope (Lowrance et al. 2000) or spectral differential imaging where the source is observed at two wavelengths (Racine et al. 1999). Another technique consists in subtracting a reference star (Boccaletti et al. 2003) as it is usually made with HST (Fraquelli et al. 2004). These methods can also be combined like in Biller et al. (2006) or in Janson et al. (2007). At the VLT, a noise reduction of 2-3 mag was obtained when combining spectral and angular differential imaging. The use of a reference star, as it will be done in MIRI obviously requires stability that might be achieved on a space telescope. Even the observation of the same target at different roll angles or in different filters will require a re-pointing onto the coronagraph. Therefore, the relative positioning of the star and the reference behind the coronagraph has to be done very accurately. The problem specificity originates from the non-linearity of the coronagraph, which prevents the use of classical algorithms to determine the centroid.

The goal of this paper is threefold with the aim to investigate :

1. the sensitivity of coronagraphic performance regarding pointing precision
2. the use of several algorithms for the pointing procedure
3. the impact of various sources of noise in the estimation of the star position

We will first briefly describe the coronagraphic system of MIRI and investigate the sensitivity in regards of the pointing accuracy in section 2. Algorithms are presented in section 3 and section 4 will be devoted to the overall study of the algorithms i.e. their systematic error (the bias) and their sensitivity to the different sources of noise. Finally, section 5 will focus on the achievable precision of the centering in MIRI as a function of the star flux.

2. MIRI Coronagraph Operation

The overall coronagraphic system of MIRI is described in details in Boccaletti et al. (2005) but the main features are reviewed here.

2.1. The coronagraphic system of MIRI

Four coronagraphs are installed in MIRI. One is a Lyot coronagraph operating at 23 μm optimized for the study of circumstellar disks, the three others are monochromatic FQPMs operating respectively at 10.65 μm, 11.4 μm and 15.5 μm. They are optimized for the detection and characterization of Jupiter-like planets (Boccaletti et al. 2005; Baudoz et al. 2006). They are associated with narrow-band filters (the spectral bandpass is 5% for the FQPMs and 20% for the Lyot coronagraph). The Lyot stops installed in the filter wheel on top of the corresponding filters, are also optimized to reduce the diffracted light while maximizing throughput.

Along this paper, we are making use of numerical simulations to assess the accuracy of pointing in the context of MIRI coronagraphic observations. Similarly to Boccaletti et al. (2005), we accounted for the telescope aperture (18 hexagonal segments), the phase aberrations of the telescope (about 130 nm RMS distributed over several spatial frequencies according to estimation from the manufacturers), defocus of MIRI with respect to the telescope focal plane, mis-alignment of the telescope pupil with respect to the Lyot stops inside MIRI, and a residual telescope jitter of 7 mas RMS. The latter, although reducing the performance, has a random statistics and therefore averages over time in contrary to the pointing accuracy we are dealing with in this paper.

2.2. Coronagraph performance with respect to the pointing

For the estimation of performance, we assume the following sequence:

1. the star is centered on the coronagraph and a long exposure is obtained.
2. Later in time, a reference observation is performed and a re-pointing is needed.

Then the performance of detection depends on two pointing parameters. The first one is the absolute pointing i.e. the positioning of the star with respect to the coronagraph. The second one is the differential positioning between the images of the target star and that of

the reference star. It is referred to pointing reproducibility. The FQPMs are obviously more demanding than the Lyot coronagraph so only the former will be considered in this study. Both parameters are analyzed in Fig. 1 considering the FQPM operating at 11.4 μm. For the FQPMs, the performances are known to vary quadratically with the errors of pointing. The situation is different here as we are dealing with differential imaging between a target and a reference. The main residual light is due to jitter and to the differential pointing of target and reference stars.

In Fig. 1 (left), the target star is located at 5 mas from the center of the coronagraph. The angular separation between the effective position of the target star and the reference star on the detector varies from 0 to 25 mas. This variation is very sensitive and critical. At $2\lambda/D$, a 10 mas separation between the target and the reference yields a loss of a factor of two in contrast. To retain acceptable performance in compliance with scientific objectives, the pointing reproducibility must be kept better than 5 mas RMS per axis as a goal. The required accuracy is then comparable to the telescope jitter (7 mas RMS for 2 axes).

In Fig. 1 (right), the angular separation between the effective position of the star and its reference on the detector is set to 5 mas. The target to coronagraph angular separation varies from 0 to 20 mas. The dependence is here less critical than for the pointing reproducibility. The requirement for absolute pointing is therefore set to 10 mas RMS per axis.

The level of accuracy requested for pointing represents $1/22^{th}$ of a pixel and $1/56^{th}$ of λ/D.

2.3. Instrumental requirement

The alignment of a star image onto a coronagraph is a very specific issue. Standard procedures are usually not applicable owing to the non-linearity of the coronagraph itself. There is certainly not a general solution and each instrumental configuration must be studied in details. A straightforward solution would be to minimize the stellar residue with respect to the off-axis image. However, this solution has many drawbacks like the diminution of the signal intensity during the centering procedure (not favorable owing to the increase of photon noise) and more important the possibility of degeneracy (especially with a FQPM) which requires the need of an appropriate model. All these refinements although probably more accurate will not be available on JWST for which on-board algorithms have to be quite simple.

For MIRI, the FQPMs, which are the most demanding, have a particular spectral transmission since they are monochromatic and therefore operate for a small range of wavelengths.

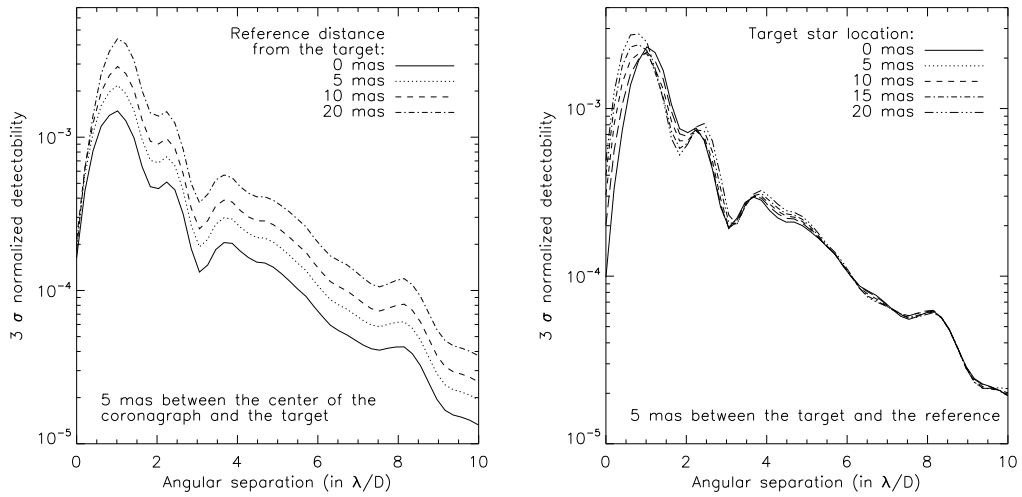

Fig. 1.— Level of detection at 3 σ for the 11.4 μm coronagraph, assuming a M2V star located at 10 pc. The residual speckle pattern is calibrated here with a reference star (similar to the star but with a different pointing). The left figure gives the contrast level if the target star is located at 5 mas from the coronagraph and the reference star location ranges between 0 and 20 mas.The right plot shows the contrast level if the target location ranges between 0 and 20 mas from the coronagraph and the calibration star is located 5 mas from the target star.

This is a characteristic that we can take advantage of since many wavelengths across the whole MIRI spectral range are leaking through the coronagraph then providing an image quite similar to a point spread function (PSF). Therefore, to preserve the linearity of the pointing procedure and to allow simple algorithms to be used on-board, it has been decided to install a Neutral Density (ND) in the filter wheel with a large spectral range and an attenuation factor finely tuned to observe as many stars as possible including the brightest.

It is not the point of this paper to describe precisely the optimization of the ND for the pointing procedure. It is however important to mention that we took into account the spectral transmission at low temperature (6.85 K) of the various elements like the optics, the FQPM (including the A/R coating) and the detector quantum efficiency (Fig. 2 left). Then, we considered one of the brightest interesting object : Vega, and the characteristics of the detector (Love et al. 2005) like the minimum integration time allowed in windowing mode (40 ms) and the full well capacity ($2 \cdot 10^5$ electrons). A polychromatic image is numerically simulated across a wide range of wavelengths (0.1 - 30 μm) larger than that of the ND itself. This is important since for instance the detector has a significant efficiency at short wavelengths (30% below 5μm). The larger the spectral range the less the FQPM will significantly affect the image and so the image during the pointing procedure will not change dramatically allowing the use of the same algorithm and settings. However, the cut-on wavelength of the ND is set by the sampling of MIRI (Nyquist at 7μm) and the cut-off wavelength is determined by the germanium transmission of which FQPMs are made. This forces the ND to be transmissive between 8 and 18μm. The dimensioning of the ND with minimal and maximal acceptable values is shown in Fig. 2 (left, dashed lines). Specifications have been defined by the following values:

- less than 10^{-6} for λ smaller than 7.6 microns;
- less than 2.10^{-3} for wavelengths between 7.6 and 8.4 microns;
- between $1.8 \cdot 10^{-3}$ and $2.2 \cdot 10^{-3}$ up to 18 microns;
- less than $2.2 \cdot 10^{-3}$ beyond.

The middle and right panels in Fig. 2 evidence the validity of the choice of the neutral density. The middle plot shows that centered and decentered images have almost the same spectrum with the neutral density in the case of Vega spectrum (the total flux with the neutral density filter is about $9.2 \cdot 10^5$ photoelectrons per second). Right panel shows on axis and off-axis images of Vega made with the neutral density: their shape is slightly different but both remain 'PSF-shaped' allowing the use of centroiding algorithms.

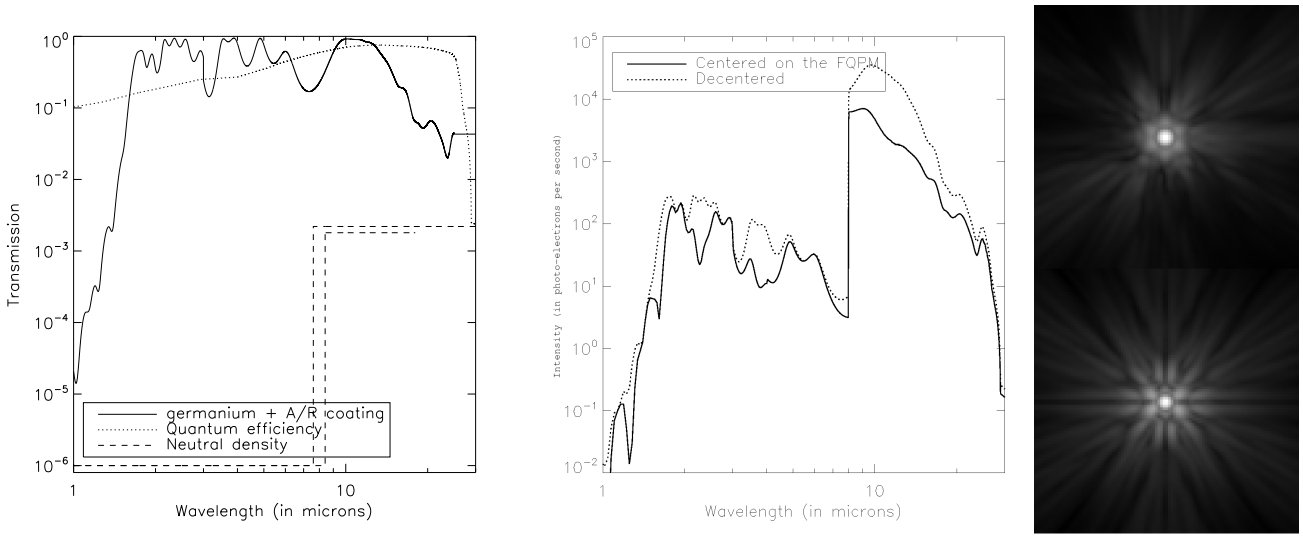

Fig. 2.— Dimensioning of the Neutral Density for accurate pointing procedure. The left panel represents the dimensions of the ND compared to the FQPM transmission and quantum efficiency, the middle one the spectrum of Vega with the ND in and out of the coronagraph and the right one the off-axis and on-axis images with the ND.

2.4. Peakup procedure

A dedicated pointing or "peakup" procedure is needed to achieve the level of accuracy given in section 2.2. As a constraint, JWST will deliver a pointing accuracy that depends on the amplitude of the offset. This accuracy is:

- 20 mas RMS per axis for offsets ranging between 2 and 20 arcsec;
- 1% of the offset amplitude for offsets ranging between 0.5 and 2 arcsec;
- 5 mas RMS per axis for offsets smaller than 0.5 arcsec.

We consider a best effort procedure. As a starting point, we assume the target star to be at 10" from the center of the coronagraphic mask (the coarse pointing of JWST). With the neutral density filter, a target location algorithm is used to locate the star. The star is moved to the center of the mask but falls within 20 mas RMS of the center while we are looking at 10 mas RMS. The target location algorithm is used again to locate the star. At this stage, the star is inside the central pixel but is very little affected by the FQPM owing to the large spectral range of the ND. If the star is at less than 10 mas from the center of the coronagraphic mask, the peakup procedure is stopped since the pointing requirement given in section 2.2 is achieved. The location of the target star is stored and the coronagraphic exposure can be started. If not, iterations are needed. For offsets smaller than 0.5" the accuracy reaches 5 mas RMS. Statistically, the star has 80% of chance to be at less than 10 mas from the center of the coronagraph in one single iteration.

The same procedure is applied for the reference star (but later in time). It has to be located within 5 mas per axis from the target star image location in the focal plane (which was stored during the target acquisition operation). The probability for the reference star to be at less than 5 mas from the target star is 35% in one iteration. Typically, about 10 iterations are needed to make sure the desired accuracy is reached. The peakup procedure is schematically illustrated in Fig. 3.

3. Algorithms for peakup

The use of a ND in MIRI to carry out the peakup procedure simplifies the problem of pointing to a "nearly" standard case. Although, there are certainly many advanced algorithms to perform fine centering of a PSF-like image taking care of the noise propagation, a first down-selection was made for MIRI based on simplicity of coding and easiness of implementation in a flight software. Another constraint is, as far as possible, to have a

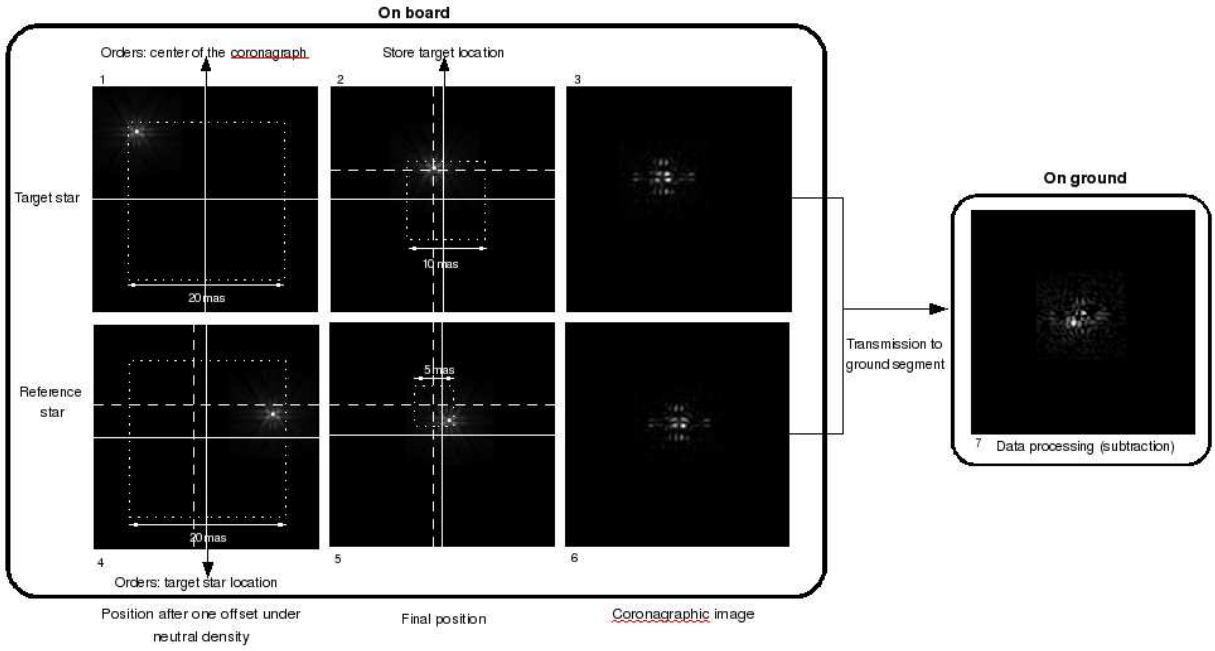

Fig. 3.— Schematic view of the peakup procedure. For clarity the scale is exagerated. The actual pixel size being 110 mas, the PSF would appear much bigger than the field of view presented here. Solid lines represents the center of the coronagraph. The first stage of the procedure brings the star/reference in a circle of 20 mas RMS (left pictures). The second stage brings the star in a circle of 10 mas (dashed lines represents the stored position of the star). The reference star has to be placed within 5 mas of this position to allow acceptable subtraction residuals.

single algorithm for the several JWST instruments. Although coronagraphy is certainly the most demanding in that regards, it is not identified as a priority for the choice of the common algorithm. Four different algorithms were considered in the following.

First, we consider the simple center of gravity (or first moment). On one axis, the expression of the center of gravity (CoG) is given by:

$$x_{CoG} = \frac{\sum_x xI(x,y)}{\sum_x I(x,y)} \tag{1}$$

where $I(x,y)$ is the intensity of the image in the pixel (x,y). The expression is identical on the other axis. As an interesting aspect the CoG is easy to implement, its sensitivity to the different noises is well known (Auer et al. 1978; Stone 1989) and it can be analytically written in the case of a gaussian image.

The second algorithm is the gaussian fitting (GFit). It is also well known and its interest resides in its robustness but as a drawback requires more complexity in coding. However, we will consider the GFit as a reference in the following since it is unbiased.

Two improved versions of the center of gravity are also considered. The floating window center of gravity (FCoG) proposed by one of us brings a solution to the known bias of the CoG (which will be studied in section 4.1). While, for the CoG, the window is always centered on the middle of the brightest pixel whatever the position of the maximum inside the pixel, the FCoG is calculated on windows centered on the maximum of the PSF. This is done by attributing a weight to each pixel at the edges of the window. For a given pixel, this weight depends on the area intercepted by the floating window. For instance the pixel at the upper left corner of the window in Fig. 4 has a weight of 60%. The left drawing of Fig. 4 shows the window used with the classical CoG. The star is not centered in the middle of a pixel. As this window only contains an integer number of pixels, the intensity is not distributed symmetrically around the star. The FCoG solves this problem. However, in the case of the FCoG, several iterations are needed:

1. at the first iteration, the window is identical to the CoG one;
2. the CoG is calculated;
3. the window is then centered on the new maximum (calculated at step 2);
4. iterate from step 2 until the result is identical to the previous iteration. A few iterations allow convergence.

Figure 4 (right) represents the window position at the last iteration.

Another algorithm derived from the CoG is the weighted center of gravity (WCoG) developed by Nicolle et al. (2004). The objective is to reduce the impact of noisy pixels and to increase the weight of pixels with a larger flux, that are pixels with more information. This is done by multiplying the image by a weighting function (gaussian, bessel, ...). The weighting function is recentered iteratively like for the FCoG. On one axis, the expression of the WCoG is:

$$x_{WCoG} = \frac{\sum_x xI(x,y)P(x,y)}{\sum_x I(x,y)P(x,y)} \tag{2}$$

with $P(x,y)$ the weighting function. In our study, we focus on a gaussian weight

$$P\left(x,y\right) = \frac{1}{\sigma\sqrt{2\pi}} e^{-\frac{(x-x_0)^2+(y-y_0)^2}{2\sigma^2}} \tag{3}$$

where $\sigma = \frac{fwhm}{2\sqrt{2\log 2}}$ with $fwhm$ the full-width at half maximum of the gaussian function. The coordinates (x_0, y_0) represents the maximum position of the gaussian function. The adopted weight is centro-symmetric.

For each algorithm, the size of the window is optimized to minimize both the bias and the impact of the noise, as explained in section 4.1.

4. Analysis of sensitivity

Two aspects have to be considered in the assessment of the algorithm sensitivity. The first one is the bias. It represents the algorithm systematic error independently of any source of noise. It is studied for each algorithm in section 4.1. The second aspect is the impact of the noise. For that purpose, several independent realizations (typically one hundred) of the noise are generated and the standard deviation between the many realizations is measured. While the overall error budget for the pointing is set to 5 mas RMS per axis, the amount attributed to the algorithm precision is only 2 mas RMS.

4.1. The bias

In this section the noise associated to the detection process (photon noise, background, flat field errors, detector noise and artifacts) is neglected in order to measure the bias only.

The GFit has in principle the great advantage to be unbiased with classical symmetric PSFs, which is no longer the case for MIRI images obtained with the ND. We measured the bias by simulating randomly distributed images inside the central pixel (Fig. 5). The dispersion of the values is 3.95 mas for the whole pixel. Meanwhile, we notice that this dispersion is getting larger far from the center of the coronagraph. For the nearest positions (<10 mas) corresponding to the final position of the star in the peakup procedure (section 2.4), the dispersion is only 0.92 mas.

The CoG is an estimator proved to be asymptotically unbiased in the case of a gaussian point spread function (Thomas 2006). In this study, it is not the case anymore, the PSF being not gaussian and the window size being finite. For the PSF of MIRI but without the coronagraph, the GFit, FCoG and WCoG are quasi unbiased (the bias is smaller than 0.2 mas) while the bias of the CoG is 3 mas RMS inside one pixel. Figure 6 left gives the CoG bias as a function of the window size for a given distance from the coronagraph. There is clearly a minimum for a 5×5 pixels window, a value that we adopt afterwards which is about identical for any positions inside the same pixel. We did not choose a larger window for which the bias can be slightly smaller because of the noise impact. According to the results presented in Fig. 6 (right) the dispersion of the bias values along the y-axis for a 5×5 pixels window is of 10.3 mas (1σ) which is not acceptable for MIRI. The bias is still too large near the center of the coronagraph (4.70 mas) and shows a specific structure. A correlation between the actual position of the star inside a pixel and the bias is evidenced in Fig. 6 (right).

For a classical PSF, the estimation can be unbiased (Yano et al. 2006). Indeed, the error on one axis only depends on the subpixel position in this axis and can be predicted. The bias origin is easy to understand: because the PSF is not exactly centered in the middle of the finite window, the intensity contained on each half of the window is not symmetrical. However, the algorithm behavior with the coronagraphic mask is not linear so the accuracy depends both on the position inside the pixel and on the distance from the coronagraph center and axes. As the position estimation variation made by the CoG is no more linear, the measure cannot be unbiased.

Two solutions are proposed. The first one is to use the FCoG which, in the case of Fig. 7, gives optimal results with a window size of 7×7 pixels. The bias is lowered to 1.5 mas. Figure 7 (right) shows the bias for different distances from the center of the coronagraph. The bias standard deviation is only 3.41 mas for the whole pixel and 0.89 mas for distances smaller than 10 mas.

The WCoG is also biased (Thomas et al. 2006) but the bias can be reduced by the same means as for the FCoG, making several iterations. At the first step the weighting

function and the window are centered on the brightest pixel. Then, the subpixel maximum is estimated by the WCoG and the weighting function as the window are recentered on this new maximum. With our hypothesis the convergence is achieved in 15 iterations.

At a position of 20 mas from the coronagraph centre, optimal result (<0.1 mas) is achieved for gaussian weighting function FWHM of 2.85 pixels (equivalent to the FWHM of the MIRI PSF) and a window size of 11×11 pixels (Fig. 8 left). For different distances from the center of the coronagraph, the bias standard deviation is 3.99 mas (Fig. 8 middle) while it is 0.96 mas for distances smaller than 10 mas.

The bias analysis is summarized in Tab.1.

4.2. Impact of noises

The goal of this section is to compare the algorithms using the optimal parameters determined in the previous section and to study the impact of the different noises. The dominant noises for the peakup procedure are :

- the photon noise of the source,
- the read-out noise,
- the photon noise of the background,
- the flat field defects.

The following figures give the pointing accuracy for the various algorithms as a function of the photon count on the detector (from 10^3 to 10^6 photoelectrons). As an example, a G0V at 10 pc represents about 5.8×10^4 photoelectrons for a 1 s exposure with the neutral density. The different sources of noise are evaluated separately except for the photon noise of the source which is always considered. Here again, the star image is obtained with the ND described in section 2.3.

4.2.1. Stellar photon noise

In this part, the coronagraphic PSF is assumed to be only corrupted by the photon noise of the target star. Figure 9 gives the pointing uncertainty as a function of the star intensity.

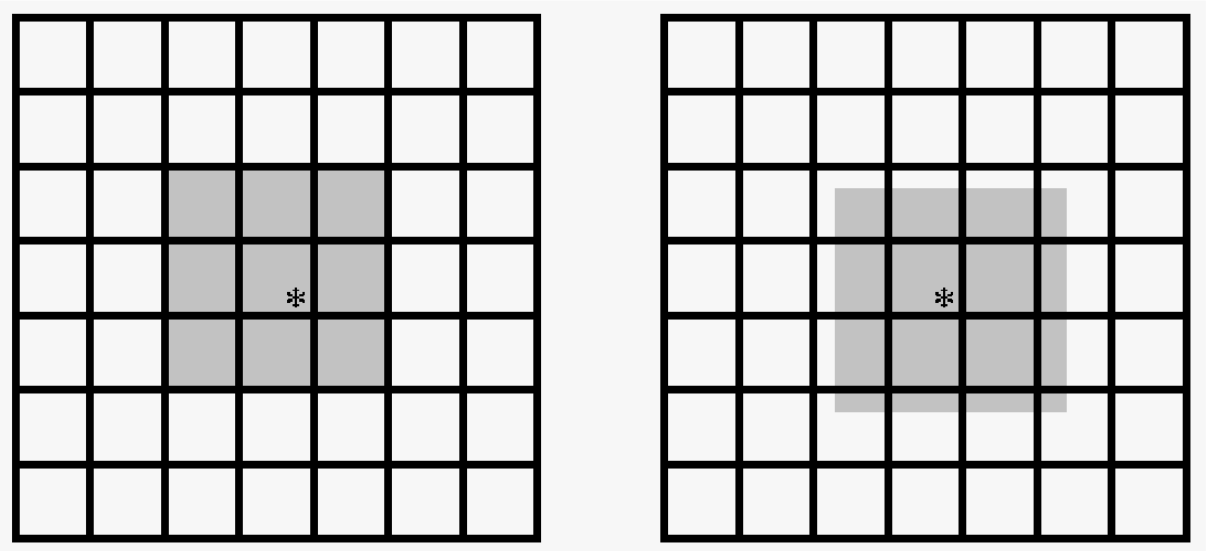

Fig. 4.— Illustration of the estimation of the position of a star in a 3×3 pixel window. The left drawing shows the classical CoG while the right one represents the window used in the FCoG.

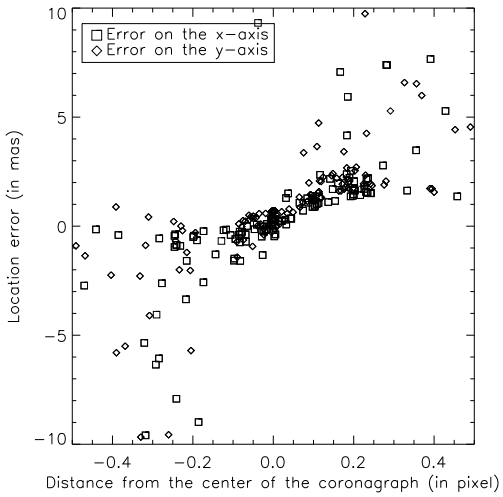

Fig. 5.— GFit bias for different positions inside the pixel.

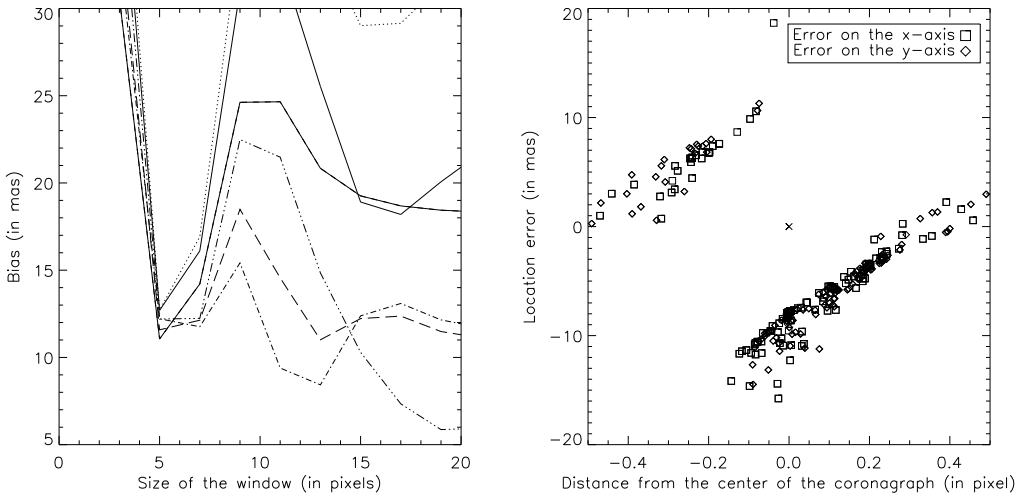

Fig. 6.— CoG bias for different parameters: the size of the window in which the CoG is calculated for different positions inside the pixel (left figure) and the position of the maximum inside the pixel for a window of 5×5 pixels (right figure).

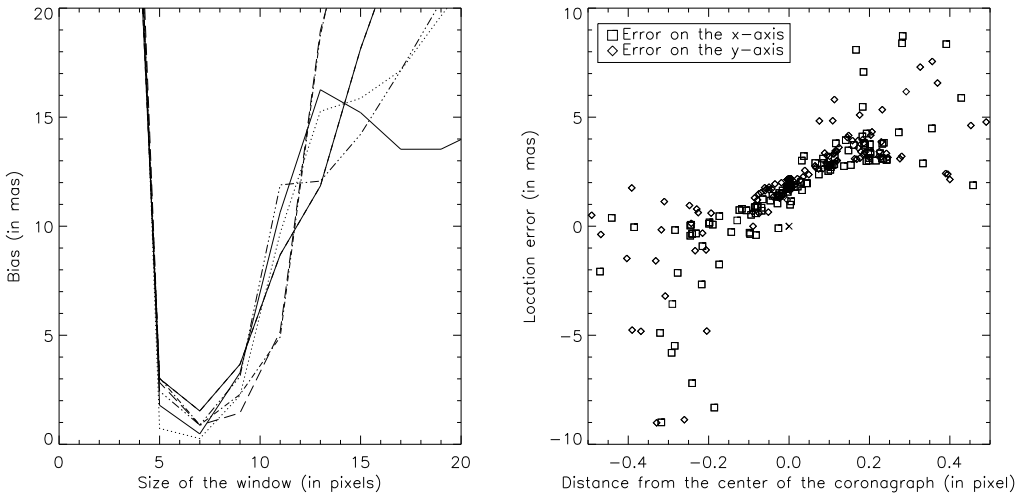

Fig. 7.— FCoG bias for different parameters: the window size (left figure) and the maximum position inside the pixel for a 7×7 pixel window (right figure).

The FCoG, WCoG and the GFit have the same behavior. The precision varies as the square root of the number of photoelectrons, in accordance with the results found in Rousset (1999) for a gaussian-shaped PSF. The reached precision is almost identical for all the algorithms.

The CoG behavior is much worse at low flux ($< 5.10^5$ photoelectrons) and the variation does not follow a simple law with a slope of -1/2. Indeed, the CoG is calculated in a box around the brightest pixel. The issue is that this brightest pixel, at low fluxes, is not always the same as without any noise: it can be either the brightest pixel itself or one of its neighbors and that creates a difference on the CoG estimation and increases the standard deviation. The effect is not the same for the FCoG and the WCoG thanks to the several iterations that prevent this effect.

To conclude, in presence of photon noise, 1.8×10^5 photoelectrons are needed to reach 3 mas RMS (radial) for the CoG, 2×10^4 for the WCoG and the GFit and only 10^4 for the FCoG. In other words, a G0V star located at 10 pc can be centered with an accuracy of 3 mas RMS in 0.22 s with the FCoG, in 0.34 s for the WCoG and the GFit and 2.76 s with the CoG.

4.2.2. Photon noise of the background

The background photon noise is another strong limitation in the mid-IR. The background flux is estimated considering the combination of several emissions from the zodiacal light, the telescope mirrors, the sunshield and that of the instrument itself. According to this model, the background with the neutral density provides 440 photoelectrons per pixel in one second. A flat background, of which the averaged value is estimated on the edge of the image, is removed. The CoG is very sensitive to the presence of a background (Nicolle 2006). Figure 10 shows that the background noise prevents the algorithms from converging at very low flux ($< 5.10^3$ photoelectrons).

For fluxes between 5.10^3 and 5.10^4 photoelectrons, the performance is 2 and 2.7 times worse than in the previous case (stellar photon noise only) for respectively the WCoG/GFit and the FCoG. For larger fluxes ($> 10^5$ photoelectrons) the performance is identical. Therefore, the impact of background noise can be overcome with a longer integration time.

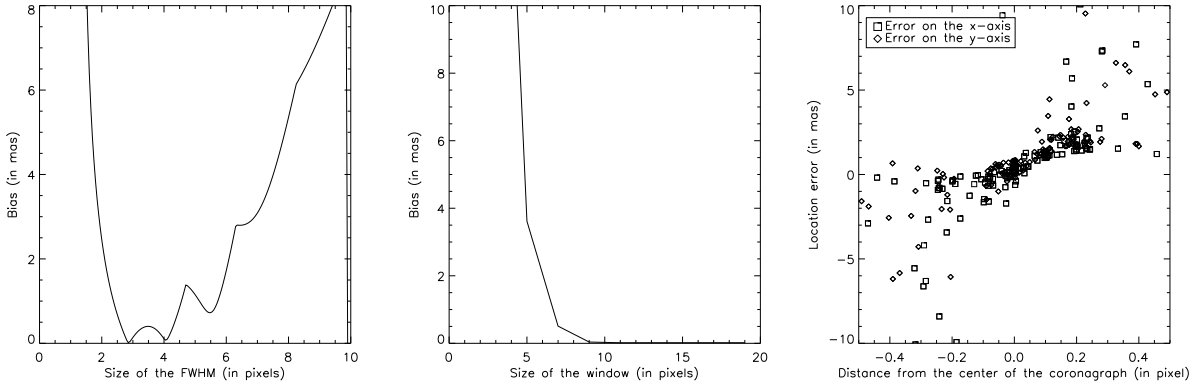

Fig. 8.— WCoG bias for different parameters: the weighting function FWHM (left), the window size (middle) and the PSF maximum position inside the pixel (right).

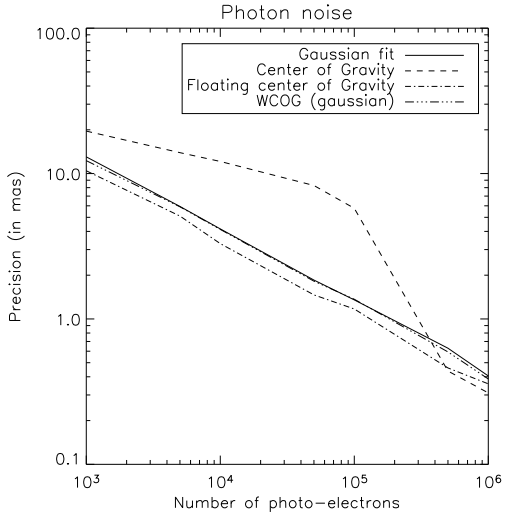

Fig. 9.— Variation of the precision of the algorithms as a function of the collected stellar flux in presence of photon noise.

4.2.3. Readout noise

In addition to intrinsic noise of the signal to be detected, the detector of MIRI also suffers from technological limitation like readout noise (RON) and pixel-to-pixel response variation. We are also aware about remanence and intra pixel response variation (of which the impact is identical to the flat field) which are not treated since not enough quantitative information is yet available. A number of other detector noises are not accounted (Pipher et al. 2004): non-linearity of the detector (here we suppose that images are acquired in the linear range), banding, ...

In Fig. 11, we study the impact of the RON for two levels, 5 and 10 e-/pixel, some expected values for the MIRI detector (photon noise of the star is also accounted for).

With 5e-/pixel, the results are quite similar to those obtained with photon noise only indicating that the RON would not be a limitation except at fluxes lower than 5.10^3 photo-electrons. The effect is more critical if the RON reaches 10e-/pixel. None of the algorithms converges at very low flux (under 5.10^3 photoelectrons) and the performances are slightly worse under 10^5 electrons. Its influence is similar to that of the background noise and therefore longer integrations are required to achieve the same precision.

Although the FCoG was better in section 4.2.1 (stellar photon noise only), this small advantage disappears for large RON values.

4.2.4. Flat field defects

In MIRI, the detector pixel-to-pixel response variation is close to 5% and can be, after correction, reduced to 1%.

The figure 12 represents the algorithm limitation in both cases. The two cases are studied because it may be difficult to calibrate precisely the flat field near the coronagraph center owing to its absorption and to the diffraction due to the FQPM step. The case of a 10% flat field is also added to estimate more accurately the influence of this parameter.

As expected, the flat field dominates at high fluxes (which means for low photon noise). This can be seen in figure 12.

At low fluxes, the pointing accuracy is limited by photon noise whatever the algorithm. With a pixel-to-pixel variation of 1% the limitation occurs at high fluxes but still a precision of 1 mas is achievable with the FCoG, WCoG and GFit. The CoG is clearly the more sensitive even at high fluxes where the pointing accuracy is reduced by a factor of 10 (for

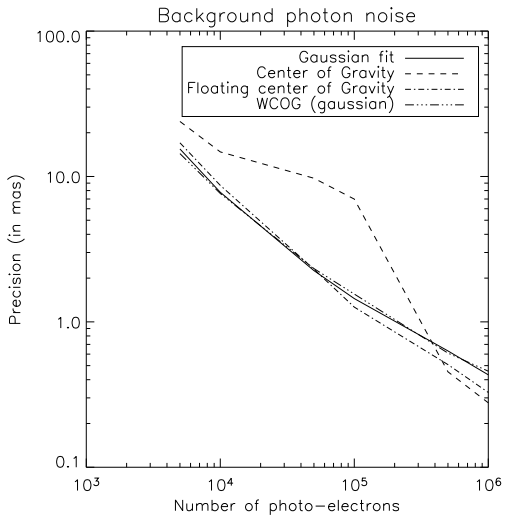

Fig. 10.— Variation of the algorithm precision as a function of the collected stellar flux with mid-infrared background.

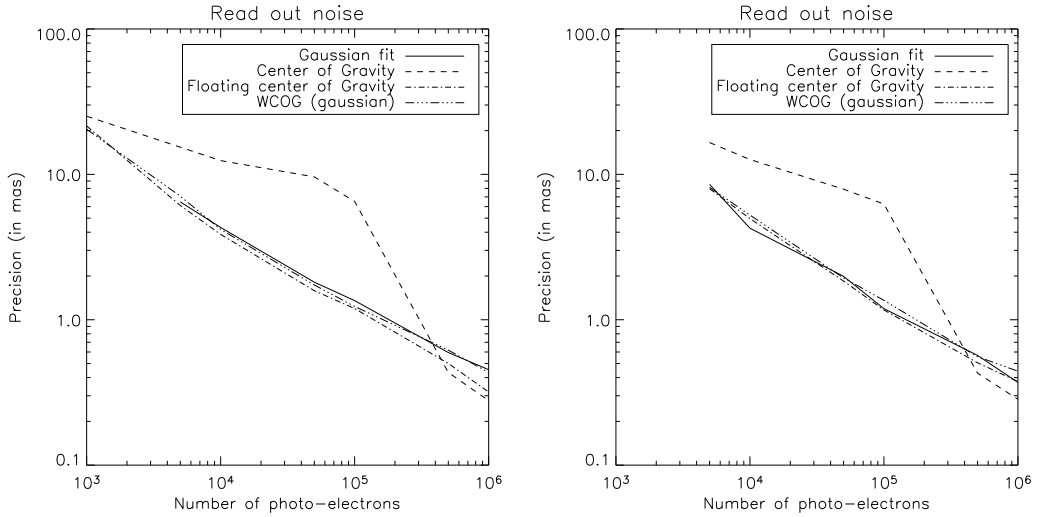

Fig. 11.— Variation of the algorithm precision as a function of the collected stellar flux in presence of read-out noise of 5 (left) and 10 electrons (right).

10^6 photoelectrons) .

The effect is more severe if no calibration is made (5% variation) with a limit at high fluxes (10^6 photoelectrons) of 10 mas for the CoG, 3 mas for the WCoG and GFit and 2 mas for the FCoG.

At 10%, the pixel-to-pixel variation is the largest error (except at low fluxes where photon noise still dominates). None of the algorithm is able to achieve the required level of 3mas RMS. So, to achieve the pointing requirements, the flat field defects must remain lower than 5% (before calibration).

However, this whole study was led assuming a varying flat field at each noise realization in order to measure the standard deviation associated to this particular noise. In MIRI, that is not the case: the flat field will be more stable so only one realization has to be accounted. The impact is different : it does not change the standard deviation but slightly changes the median value.

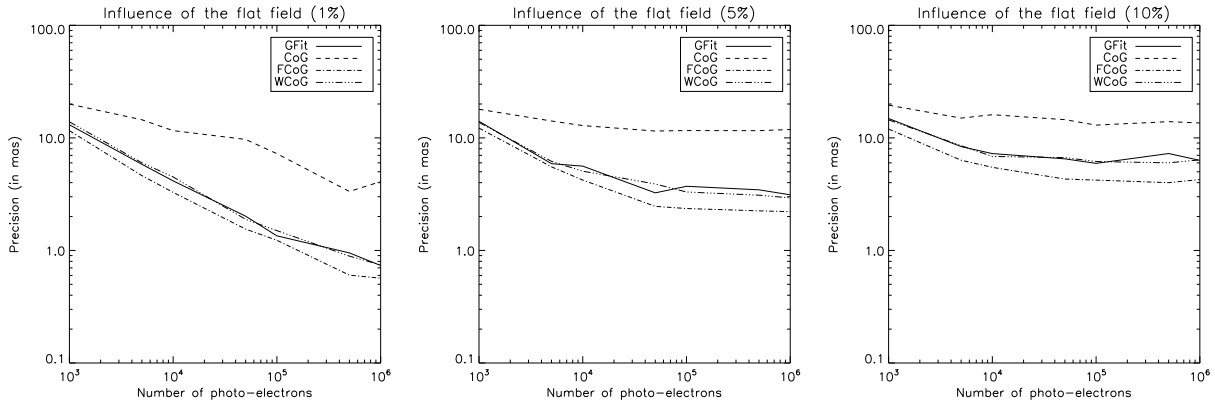

Fig. 12.— Variation of the algorithm precision as a function of the collected stellar flux with flat-field defects of 1%, 5% and 10%.

4.3. Conclusions on the algorithm sensitivity

Four algorithms were studied for the coronagraphic peakup procedure using a noise model that is representative to that of MIRI.

The gaussian fitting is difficult to implement in a flight software so it has to be excluded.

The center of gravity produces a bias which is beyond the requirement for accurate pointing onto the coronagraph and this cannot be corrected. In addition, at low fluxes it is performing worse than other algorithms.

The CoG using floating windows is little biased and easy to implement. Its performances are also acceptable in presence of noise. Its only drawback is the need for several iterations to be efficient.

Finally, the weighted CoG produces similar results to that of the FCoG and of the gaussian fit. It is also little biased and easy to implement, but an additional parameter is needed.

Results are summarized in Tab. 1. The FCoG is the one that reaches the best accuracy in agreement with pointing requirements.

In the following, the CoG is not considered anymore because its performances are insufficient.

	Gaussian fitting	CoG	WCoG	FCoG
Bias	0.92	4.70	0.89	0.96
Photon noise	1.2	5	1.2	1.05
Photon noise + RON (10 electrons)	1.05	6	1.2	1.05
Photon noise + background photon noise	1.3	7	1.3	1.1
Photon noise + Flat field defects	4	10.2	3.1	2.1

Table 1: Precision of the algorithms (in mas RMS) for the different sources of noise and the bias assuming a total stellar flux of 10^5 photoelectrons. The budget error attributed to the algorithms is 3 mas RMS for the 2 axes.

5. Global performance on MIRI

The global performance of the algorithms is now studied with all the dominant noises described in the previous section. We are considering photon noise (object and background), a RON of 10 electrons per pixel and a pixel to pixel uniformity of 5%. The bias is also accounted for.

Figure 13 left gives the algorithm precision for G0V and M0V stars at 10 pc, as a function of the exposure time. The algorithms have similar performances. The bias impacts identically all the algorithms: for long integration time the accuracy converges to a value of about 1 mas. The limit is reached faster for a G0V than for a M0V given the difference of brightness. Therefore, beyond 20 s, it is useless to increase the exposure time. To achieve a pointing precision of 3 mas, an integration time of 0.6s is needed to perform centroiding measurement on a G0V star at 10pc while it amounts to 10s for a M0V star.

Using these simulations, it is thus possible to estimate the time necessary to reach the required precision (3 mas radially) as a function of the flux of the star (Fig 13 middle). For G0V stars closer than 20 pc, the exposure time can be retained smaller than one minute. However, M0V stars are about 6.4 times fainter than G0V stars at mid-IR wavelengths which mean that for the same exposure time the sample of M0V targets is limited to a distance of 7.9 pc. The exposure time will become prohibitive and raises some stability issues for fainter stars. It is of course desirable to get further away to observe fainter stars. The ND attenuation is too large for faint stars but another filter can be used. This filter must to be different than the operating wavelength of the coronagraph to reduce the coronagraphic effect and to allow centroiding. In the case of MIRI and the FQPM at 11.4 μm, it is possible to perform the peakup procedure with the N band filter of the imager mode ($\lambda = 9\mu m$, $\Delta\lambda = 2\mu m$). Figure 13 right gives the required exposure time to reach 3 mas as a function of the distance of the star with the N band filter. A star of 9 magnitudes in the N band filter (for instance a G0V star at 100 pc or a M0V star at 63 pc) can be centered in less than 10 s. Therefore, the N filter is well suited to centering faint stars with the 11.4 μm coronagraph and is complementary to the ND filter.

These results prove the interest of the WCoG and the FCoG for the positioning behind the FQPM of MIRI. Besides, they show that a star, even faint ones, can be centered accurately in a reasonable amount of time.

6. Conclusion

To reach its scientific objectives, MIRI needs to use a coronagraph. To comply with the required performances, we have set the specifications on the pointing and on the reproductibility: the target star must be located at 10 mas from the center of the coronagraph and the reference must be at less than 5 mas from the target star.

Here, the specificity of the centroiding comes from the non-linearity of the coronagraphs. So a specific study was carried out to assess the best procedure in this context and to evaluate the feasibility. Different algorithms were compared in the case of MIRI. The classical center of gravity was proved inefficient for this purpose. Two solutions derived from the center of gravity are the floating center of gravity and the weighting center of gravity which provide almost unbiased measures in a reasonable amount of time. This study allows us to put specifications on the different noises, mainly on the flat field uniformity which must not exceed 5% RMS.

We also demonstrated that stars as faint as magnitude 9 in N band can be accurately centered onto the coronagraph in less than 10 s. This point is particularly important for MIRI: indeed, faint stars are the most numerous targets. A statistical analysis to be published in a forthcoming paper proves that the characterization of massive exoplanets is more likely around these late type stars.

To validate the imager of MIRI, a telescope simulator is being developed at CEA/Saclay in France. It includes a warm telescope and a cryogenic enclosure which contains the imager. As for the coronagraph we will be able to test with the actual MIRI optical setup the performance in terms of contrast but we will also evaluate the feasibility of the peakup procedure and study the limitations. The first coronagraphic tests are foreseen in mid 2008.

REFERENCES

Auer, L. H. , Van Altena, W. F. 1978,AJ, 83, 531

Baudoz, P., Boccaletti, A. , Riaud, P. , Cavarroc, C. , Baudrand, J. , Reess, J. M. , Rouan, D. 2006, PASP, 118, 765

Biller, B. A., Kasper, M., Close, L. M., Brandner, W., Kellner, S. 2006, ApJ, 641, L141

Boccaletti, A., Riaud, P., Rouan, D., Baudrand, J. 2003, EAS Publications Series, Volume 8, 2003, Astronomy with High Contrast Imaging, Proceedings of the conference held 13-16 May, 2002 in Nice, France. Edited by C. Aime , R. Soummer, 8, 159

Boccaletti, A., Baudoz, P., Baudrand, J., Reess, J. M. Rouan, D. 2005, Advances in Space Research, 36, 1099

Fraquelli, D. A. and Schultz, A. B. and Bushouse, H. and Hart, H. M. and Vener, P., PASP, 116, 56

Janson, M., Brandner, W., Henning, T., Lenzen, R., McArthur, B., Benedict, G. F., Reffert, S., Nielsen, E., Close, L., Biller, B., Kellner, S., Günther, E., Hatzes, A., Masciadri, E., Geissler, K., Hartung, M. 2007, AJ, 133, 2442

Love, P. J. and Hoffman, A. W. and Lum, N. A. and Ando, K. J. and Rosbeck, J. and Ritchie, W. D. and Therrien, N. J. and Holcombe, R. S. and Corrales, E. 2005, Proc. SPIE, 5902, 58

Lowrance, P. J., Schneider, G., Kirkpatrick, J. D., Becklin, E. E., Weinberger, A. J., Zuckerman, B., Plait, P., Malmuth, E. M., Heap, S. R., Schultz, A., Smith, B. A., Terrile, R. J., Hines, D. C. 2000, ApJ, 541, 390

Nicolle, M. , Fusco, T. , Rousset, G. , Michau, V. 2004, Optical Letter, 29, 2743

Nicolle, M., PhD, Université de Paris-XI

Pipher, J. L. and McMurtry, C. W. and Forrest, W. J. and et al. 2004, Proc. SPIE, 5487, 234

Racine, R., Walker, G. A. H., Nadeau, D, Doyon, R., Marois, C. 1999, PASP, 111, 587

Rouan, D., Riaud, P., Boccaletti, A., Clénet, Y., Labeyrie, A. 2000,PASP, 112, 1479

Rousset, G. 1999, Adaptive Optics In Astronomy, 91

Stone, R. C. 1989, AJ, 97, 1227

Thomas, S. 2006, PhD, Université de Nice Sophia-Antipolis

Thomas, S. , Fusco, T. , Tokovinin, A. , Nicolle, M. , Michau, V. , Rousset, G. 2006, MNRAS, 371, 323

Yano , Araki, H. , Gouda, N. , Kobayashi, Y. , Tsujimoto, T. , Nakajima, T. , Kawano, N. , Tazawa, S. , Yamada, Y. , Hanada, H. , Asari, K. , Tsuruta, S. 2006, PASP, 118, 1448

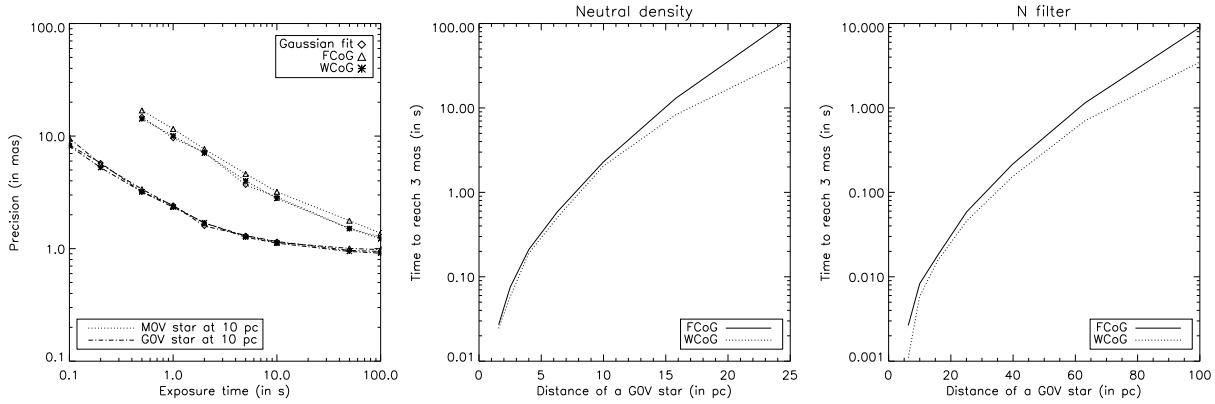

Fig. 13.— Centering algorithm performances. The left figure represents the centering algorithm performances on MIRI for a G0V star (dashed line) and a M0V star (plain line) located at 10 pc. The time required to reach a 3 mas precision as a function of the distance of a G0V star with the neutral density is plotted in the middle, the time required to reach a 3 mas precision as a function of the distance of a G0V star with the filter N in the right figure.